2D Materials

CrossMark

Graphene films printable on flexible substrates for sensor applications

Indrani Banerjee[1,2], Tsegie Faris[2,3], Zlatka Stoeva[3], Paul G Harris[2], J Chen[2], Ashwani K Sharma[4] and Asim K Ray[2]

[1] The Department of Physics, Birla Institute of Technology, Mesra, Ranchi-835215, India
[2] Institute of Materials and Manufacturing, Brunel University London, Uxbridge, Middlesex UB8 3PH, UK
[3] DZP Technologies Limited, Future Business Centre, Kings Hedges Road, Cambridge CB4 2HY, UK
[4] United States Air Force Research Laboratory, Space Vehicles Directorate, SE Kirtland AFB, NM 87117 USA

E-mail: asim.ray@brunel.ac.uk

Abstract

Fifteen-layered graphene films have been successfully deposited onto flexible substrates using a commercial ink consisting of graphene particles dispersed in an acrylic polymer binder. A value of 74.9×10^5 cm^{-2} was obtained for the density of defects, primarily located at the flake edges, from the ratio of the D and G Raman peaks located at 1345 cm^{-1} and 1575 cm^{-1} respectively. 0.5 μm thick drop-cast films on interdigitated silver electrodes exhibited Ohmic conduction with a small activation energy of 12 meV over the temperature range from 260 to 330 K. The photo-thermoelectric effect is believed to be responsible for photoconduction through graphene films under illumination intensity of 10 mW m^{-2} at 270 nm, corresponding to the UV absorption peak. The photo-transient decay at the bias of 1 V involves two relaxation processes when the illumination is switched off and values of 8.9×10^3 and 4.3×10^4 s are found for the relaxation time constant using the Kohlrauch stretched exponential function analysis.

1. Introduction

The mechanical, electrical, and optical properties of graphene are outstandingly promising for exploitation in the wide range of possible applications such as field effect transistors, sensors, for flexible and wearable electronics [1–3]. Successful mechanical exfoliation of highly oriented pyrolytic graphite sample to produce thin layers of graphene has been reported in 2004. A one atom thick single layer graphene consists of sp^2-hybridised carbon atoms arranged in a hexagonal lattice. The overlap between the conduction and valence bands is found to occur in ambipolar, mono-crystalline thin films showing a large carrier concentration of 10^{17} cm^{-2} and high mobility up to 10 000 cm^2 V^{-1} s^{-1} [4]. Mechanical exfoliation and chemical vapour deposition (CVD) are commonly used to synthesise high quality graphene films, often in conjunction with high temperature annealing to reduce the number of defects [5]. Few-layer graphene was grown on a catalyst copper foil substrate by controlled thermal evaporation of polystyrene carbon source under atmospheric pressure [6]. The semi-metallic properties of zero band-gap and zero local density of states at the Fermi level limit the significant applications of pristine graphene in nanoelectronics. Boron and nitrogen atoms are extensively used as doping agents for graphene because of their similarity with carbon atoms in atomic size. Nitrogen doping in high concentration contributes electrons to delocalised states of graphene, causing the shift of the Dirac energy [7]. The choice of doping strategies is very important to achieve stable performance of the device over time. Stable, high transparency has been achieved for CVD multilayer graphene doped with ferric chloride and tin (II) chloride [8]. Transverse electric fields are applied to the sample for tuning band gap without involving any chemical doping. For example, values of 250 meV and 1000 cm^2 V^{-1} s^{-1} were obtained for tuneable band gap and mobility for an exfoliated graphene bilayer used in a dual gate field-effect transistor configuration between gold top and platinum bottom electrodes [9].

Printing is regarded being as an alternative, economically viable technique for producing micro-patternable conductive graphene films at room temperature over large area on flexible substrates under ambient conditions without using vacuum or inert atmospheres. Graphene electrodes having low sheet resistance of 0.3M $\Omega/\square$ and high optical transparency in the order of 86% has been successfully fabricated by photothermal reduction of inkjet printed graphene oxide sheets using the IR heat lamp in ambient environment for about 10 min [10]. The challenge with printing graphene is in formulating the ink since the various rheological properties such as density, surface tension and viscosity have a strong effect on the printing process. Low boiling point and environmentally-friendly solvents, such as ethanol and water in the volume ratio of 1:1 gives a surface tension of $\sim$31 m Nm^{-1} which meet the requirement of producing graphene- and few-layer graphene-based inks [11]. If the graphene loading is too low, below the percolation threshold of the system, then there will be no conductivity. A key advantage of graphene is its high aspect-ratio, flake-like, structure which will result in a much lower threshold than if it were low aspect-ratio morphology. Above the percolation threshold the conductivity will improve slightly as the loading is increased, but at the expense of the coating's mechanical properties, such as flexibility and extensibility. Poor mechanical stability can lead to cracks in the films and a loss of conductivity. The nature of the binder material is also critical in determining the flexibility of the deposits [12]. The liquid-phase exfoliation methods suffer from poor controllability in size and thickness, poor production efficiency and dispersion instability. The shear exfoliation technique is recently reported to be faster than liquid-phase exfoliation methods and therefore is regarded as being scalable for mass production using commercially available inkjet printers ranging from desktop to roll-to-roll. The graphene ink (GI) is formulated with the graphene dispersion through tuning the viscosity by adding ethylene glycol using a mild sonication process. During the process, ethyl cellulose is added as stabiliser in order to keep the shear exfoliated graphene flakes stable inside the ink. The resulting few layer graphene films are highly conductive and stable over several months [13]. Graphene flake size should be fifty times smaller than the printing nozzle diameter. The flake size can be controlled by fluorination of multi-layered graphene flakes in suspension of 3% aqueous solution of hydrofluoric acid [14]. The aerogel is fabricated by combining drop-on-demand 3D printing and freeze casting into continuous, boundary free microstructure for 3D architectures [15].

We have recently reported a positive value of 1.5×10^{-3} K^{-1} for the temperature coefficient of resistance for printed 0.5 μm thick graphene films on flexible plastic substrates, over the temperature range from 260 to 330 K [16]. In light of this preliminary observation, further work has been undertaken to investigate the scope of fabricating low cost graphene thermistors and UV photosensors, using this material. A number of earlier studies have focused on the use of graphene in hybrid architectures for photodetector devices [17]. This article presents the results of an investigation into the photocurrent transient relaxation behaviour, of simple graphene films, that can be printed over large area and on flexible substrates. Raman Spectroscopy, Scanning Electron Microscopy (SEM) and UV–Visible spectroscopy studies have been carried out on graphene films, in an effort to get a better understanding of the material's structure and morphology, and hence shed light on its interesting electrical properties.

2. Experimental procedure

The commercially available ink from DZP technologies Ltd (product number G087) was formulated with few-layer graphene particles of lateral dimensions <40 μm, obtained by liquid phase exfoliation. The graphene particles were then dispersed in an acrylic polymer binder system to obtain the ink suitable for deposition on polyethylene terephthalate (PET) substrates (Melinex DuPont Teijin). Organic binding additives are not normally used in graphene films deposited for example by CVD processes. The ink used in this work is specifically formulated for industrial, large area printing and coating methods such as slot-die, gravure and flexography which are high-speed, volume manufacturing processes. However, the samples for electrical measurements consisted of drop cast GI films, 0.5 μm in thickness (t), on predesigned interdigitated silver electrode structures, on PET substrates. The dropcast method was chosen here for the small scale, rapid deposition and the ink was mixed using high-speed mixer immediately before dropcasting using a micro-pipette with a view to ensuring a high degree of the film uniformity and reproducibility. This interdigitated electrode structure has been chosen in order to facilitate direct illumination on an enlarged photodetection area. A Keithley 617 electrometer in the microprocessor controlled measuring system was employed to record both dark current and photocurrent characteristics as a function of bias voltage V for the drop cast samples, which were held under vacuum of 10^{-5} mbar in an Oxford Instrument liquid nitrogen constant bath cryostat. The mechanical stability of the graphene coating was investigated by measuring the room temperature resistance of drop cast films, on 0.1 mm thick PET substrates between two planar silver electrodes at the ends of the film GI under both extension and compression conditions of bending. The PET substrate was much longer than the GI film in order to apply uniform stress on the GI film.

A monochromator (HR320 Jobin-Yvon, HORIBA) was used as a light source in the spectral range of
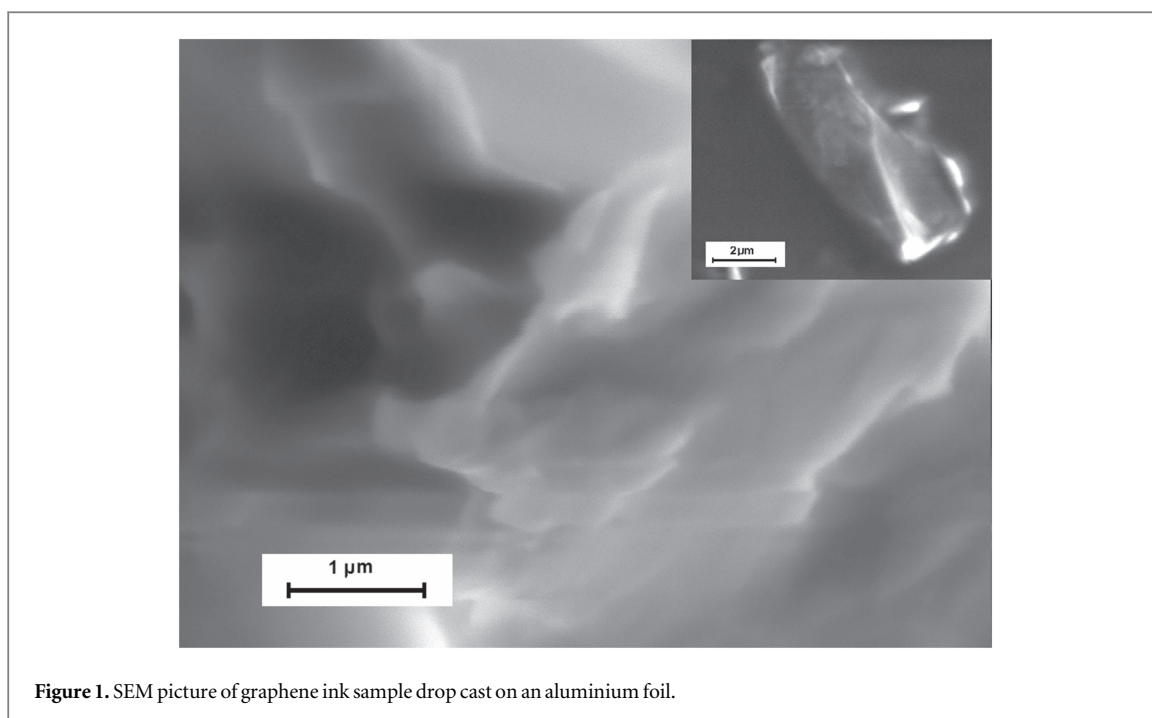
Figure 1. SEM picture of graphene ink sample drop cast on an aluminium foil.

300–700 nm for photoconduction experiments. UV–visible absorption spectra of the printed film on quartz substrates were recorded using a Perkin-Elmer LAMBDA 650 spectrophotometer between 190 and 900 nm scanning at the rate 654.8 nm min^{-1}. The surface microstructure of the GI drop-cast on an aluminium foil was investigated using an S3400N scanning electron microscope. The samples were characterised by means of x-ray diffraction using Bruker D8 advance scanning instrument. Cu K$_\alpha$ radiation of wavelength 0.15406 nm was used with scattering angle varied between 10° and 90° at scanning rate of 0.02° per sec for crystallographic analysis of the samples. The Raman spectra were obtained by Horiba Jobin Yvon Lab RAM HR800 with incident laser beam of wavelength 514.5 nm (equivalent to the excitation laser energy $E_L = 2.41$ eV) of 2 μm spot size.

3. Results and discussions

Experimental results are analysed in order to derive physically meaningful information regarding lattice structure, defect type and density, and electrical and optical device parameters. Values of material parameters have been compared with relevant published data for identifying new knowledge.

3.1. Microstructural, crystallographic and compositional studies

Figure 1 shows a scanning electron micrograph of the graphene deposit. It is apparent that the lateral dimensions of the flakes are in the micrometre range, although of course their thickness is three orders of magnitude smaller. Such materials pose challenges for this form of microscopy because the thickness of the flakes is massively smaller than the penetration depth of the electron beam used, and is even small compared to the range of secondary electrons used to form the image. As a result the three-dimensional structure of the whole near surface contributes to the image, rather than the normal situation when the image is dominated by the topography of the outermost surface. Additionally, the backscattered electron and secondary yields of graphene are both extremely low [18], and so ultimate resolution must be compromised in order to achieve sufficient signal to form an image.

The XRD spectrum in figure 2 of the sample shows a strong and sharp [002] peak at 26.19° corresponding to an interlayer distance of $d_{002} = 0.34$ nm determined using Bragg's law, where the subscript (002) refers to the diffraction plane. These results are in good agreement with those obtained for exfoliated graphite oxide precursor after electrochemically reduction at 1.5 V, and are close to those for pristine graphite [19]. A value of 5.57 nm is estimated for the average crystallite size, D_{002}, from the Debye–Scherrer formula in the form:

$$D_{002} = \frac{0.94\,\lambda}{\beta \cos\theta}, \qquad (1)$$

where the value of the full width at half maximum (FWHM) $\beta = 1.5°$ is found from figure 2.

The number of graphene layers N_{GL} is estimated to be 15 from the expression $D_{002} = (N_{GL} - 1)d_{002}$ assuming D_{002} represents the thickness as measured from the centre of the sample. The stacking of these layers is responsible for the intensity and sharpness of the [002] peak [20]. The additional weak peak at $2\theta = 13°$ due to the reflection from [010] plane implies the presence of residual oxygenated functional groups with interlayer spacing of 0.68 nm in the crystalline matrix of GI [21].
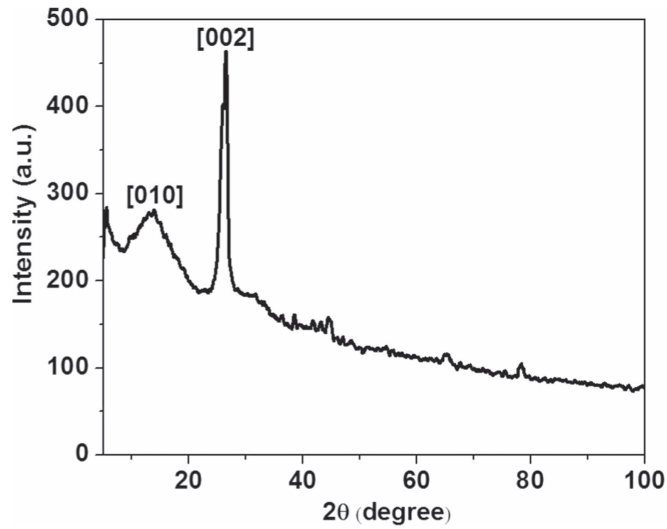
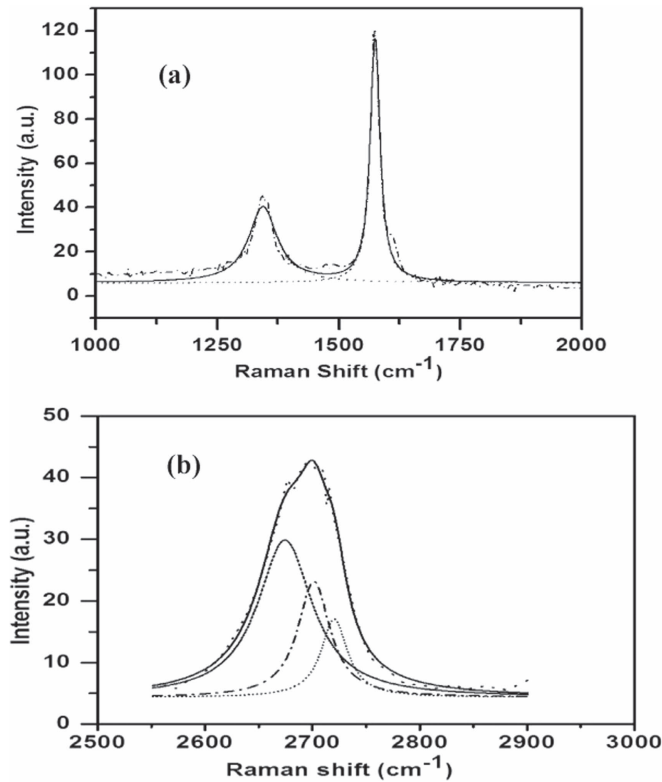**Figure 2.** X-ray diffraction spectrum of the drop-cast ink on an aluminium foil.

Figure 3. Raman spectrum for the graphene ink sample drop-cast on aluminium foil for (a) 1000 cm^{-1} $\leqslant \lambda^{-1} \leqslant$ 2000 cm^{-1} and (b) 2500 cm^{-1} $\leqslant \lambda^{-1} \leqslant$ 3000 cm^{-1} fitted with three Lorentzian components.

The Raman spectra in figure 3 for the GI sample were recorded for the wavenumbers ranging from 1000 to 3000 cm^{-1}. The characteristics peaks of D and G have been observed at 1345 cm^{-1} and 1575 cm^{-1} respectively in figure 3(a). These peak positions are in agreement with those observed for the annealed graphene layer ink-jet printed on a Si/SiO$_2$ substrate [22]. The D band is due to the breathing modes of sp^2 rings of six-atom rings. The intense G band arises from in-plane vibration of sp^2 carbon atoms present in the

sample [23]. The intensity ratio of I_D/I_G is found to be 0.3, reflecting the defect concentration of carbonaceous materials [24]. A value of 20.6 nm is estimated for an average inter-defect distance L_D in nm using the relation [25]:

$$L_D{}^2 = \frac{4.3 \times 10^3}{E_L{}^4}\left[\frac{I_D}{I_G}\right]^{-1}, \qquad (2)$$

where E_L = 2.41 eV is the laser excitation energy. Although the spot size is nominally 2 μm, the laser beam is expected to penetrate into the depth of
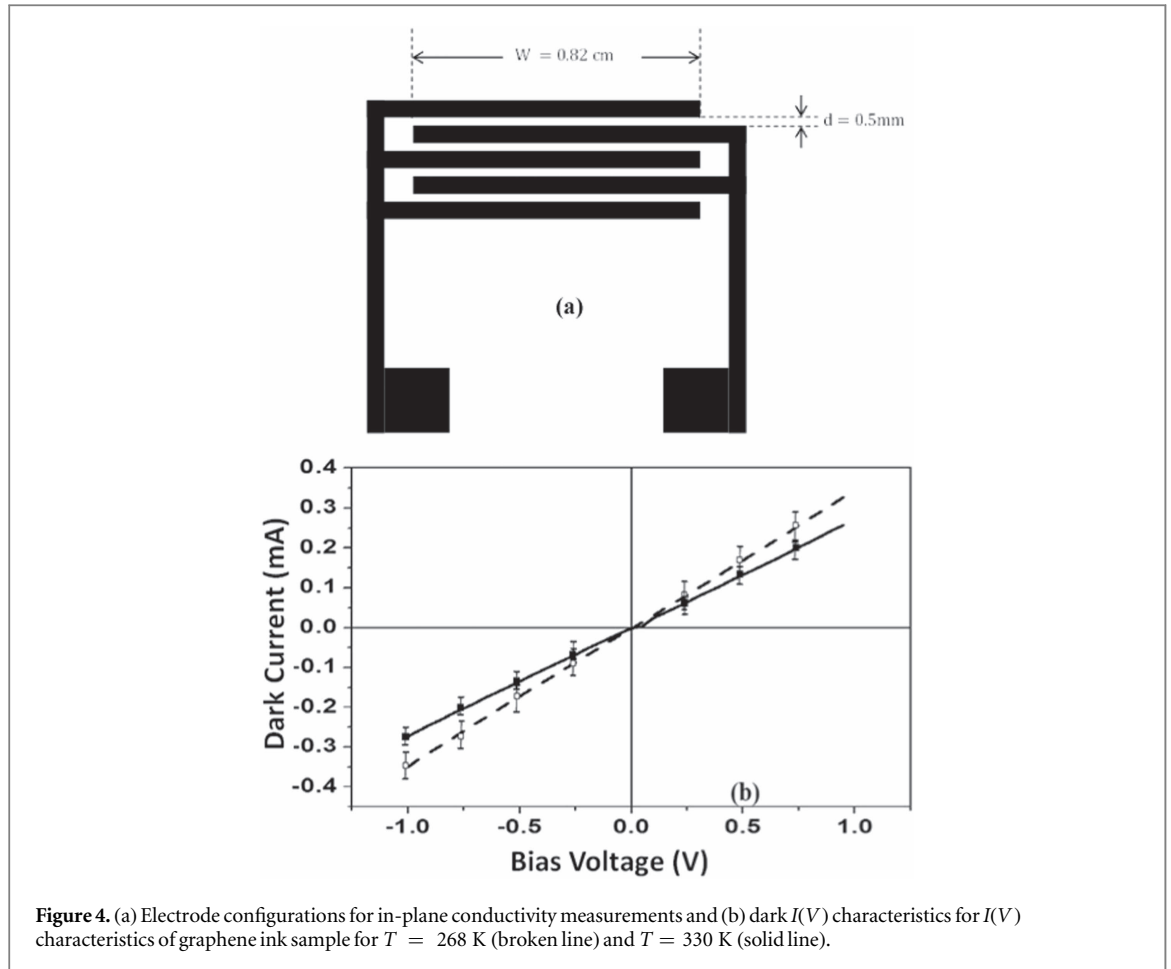
Figure 4. (a) Electrode configurations for in-plane conductivity measurements and (b) dark $I(V)$ characteristics for $I(V)$ characteristics of graphene ink sample for $T = 268$ K (broken line) and $T = 330$ K (solid line).

>50 nm encountering a large number of graphene flakes. Therefore, the estimated value of L_D is considered to be reasonable in the context of the scattering within a large volume [26]. The value of 74.9×10^5 cm^{-2} is found for the defect density n_D from the knowledge that $n_D{}^2 = \frac{1}{(\pi L_D{}^2)}$. These defects are believed to be located at the flake edges responsible for activation by double resonance giving rise to the D peak. Figure 3(b) shows that a broad $2D$ peak due to absorptions by second order zone-boundary phonons appears at 2690 cm^{-1}, representing a blue-shift by $\sim$30 cm^{-1} in relation to monolayer samples [27]. Also, a value of 80 cm^{-1} for the FWHM of the $2D$ peak is approximately three times larger than that reported from single layer graphene. These observations are consistent with earlier XRD studies that the sample is multi-layered. This $2D$ peak, usually referred to as a second-order overtone of the D peak, is not assigned to the defects for their activation since its origin is attributed to the momentum conservation by two phonons with opposite wave vectors. However, the positions of both D and $2D$ peak are dispersive dependent on the laser excitation energy. Figure 3(b) also illustrates an analysis of the $2D$ peak envelope, assuming a Lorentzian peak shape. Three components are found to fit the envelope with their peaks to be located at 2675, 2700 and 2725 cm^{-1}.

3.2. Steady state electrical measurements

As shown in figure 4(a), in-plane dc conductivity measurements were made using the interdigitated electrode systems with dimensions of $d = 0.5$ mm, $W = 0.82$ cm and $N = 5$, where d, W and N are the distance between the fingers, the overlapping width and the number of fingers in the electrode system, respectively. Figure 4(b) shows the current I versus bias voltage V plots for the sample at $T = 268$ K and $T = 330$ K. These $I(V)$ characteristics are linear within the bias voltage regime, implying the Ohmic nature of conduction. The dark Ohmic conductivity σ_D of the GI sample is estimated to be 1642 ± 123 S m^{-1} at 268 K from the relation:

$$\sigma_D = \frac{1}{R_D} \frac{d(N-1)}{t.w}. \tag{3}$$

Values of dark Ohmic resistance R_D were determined from the slope of individual $I(V)$ plot in figure 4(a). This value of $\sigma_D = 1642$ S m^{-1} compares well with one observed for a printed 0.22 μm thick multi-layered graphene film which was annealed at 400 °C. The ink was produced from ultrasonicated ozone modification of aqueous dispersions containing exfoliated graphite [28]. Similarly a value of 1231 ± 117 S m^{-1} was obtained for σ_D at 330 K. A
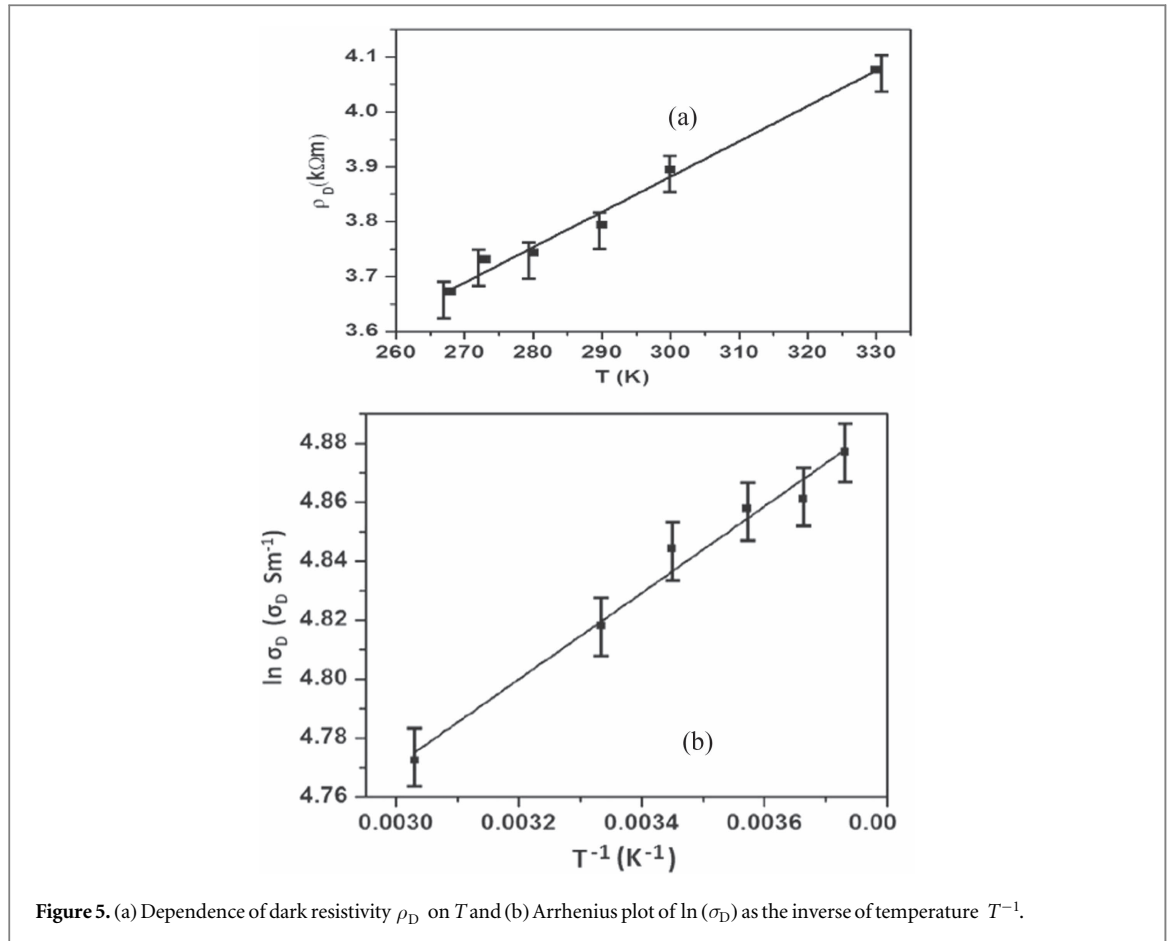
Figure 5. (a) Dependence of dark resistivity ρ_D on T and (b) Arrhenius plot of ln (σ_D) as the inverse of temperature T^{-1}.

comparable value of 1100 S m^{-1} for the room temperature conductivity is reported for a ∼25 nm thick film spin-coated with dispersions of few layered graphene in N,N-dimethylformamide (0.7 mg ml^{-1}) solvent [29]. However, the resistivity of thin printed samples of UV-driven water-based graphene oxide/acrylic poly(ethylene glycol) diacrylate nanocomposite is reported to vary between 10^4 and 10^6 Ωm with the increase in the film thickness from 4 to 12 μm [30]. This shows the drop cast film of the present investigation is considerably more conducting than these nanocomposites.

Four further measurements were carried out at temperatures between 268 and 330 K and the dependence of the dark resistivity ρ_D on T is shown in figure 5(a). This behaviour of ρ_D (T) can be described by a simple well-known relation in the form:

$$\rho_D = \rho_{D0} [1 + \propto T], \qquad (4)$$

where ρ_{D0} and α denote the resistance at 0 K and the temperature coefficient of resistivity of the GI sample. The ratio of the slope to the intercept at $T = 0$ K gives $(3.07 \pm 0.12) \times 10^{-3}$ K^{-1} for the temperature coefficient α. This value is larger than one reported for graphene nanowalls by an order of magnitude [31]. It is, however, within the same order of magnitude as other highly conducting materials such as copper and silver [32]. The existence of positive temperature coefficient may be attributed to an increase in the

interlayer distance with the rise of temperature, thereby reducing the tunnelling current between the layers [33]. The contributions of both optical phonons and intervalley scattering by transverse and longitudinal modes become increasingly significant with rising temperature [34]. The value of the activation energy ΔE is estimated to be 12 meV from the slope of Arrhenius plot in figure 5(b) of ln (σ_D) as the inverse of temperature T^{-1}. $\Delta E = 12 \pm 1.5$ meV represents a non-zero band gap between the conduction and valence band and it is smaller than room temperature thermal energy. The small value of $\Delta E = 12$ meV in the present work implies the possible break up of lattice symmetry at the Dirac points (**K**) of the graphene films due to the presence of defects [35]. This observation is consistent with our earlier observations from Raman and SEM studies. ΔE is generally sensitive to the measurement environment such as the presence of moisture, local humidity and the hydrophobicity of the binder resin. A value of $\Delta E = 29$ meV which is almost equal to thermal energy is reported for CVD deposited graphene films from Van Der Pauw conductivity measurement in vacuum for the comparable temperature range [36]. Both temperature coefficient and activation energy have been measured for graphene flake- and solar exfoliated reduced graphene within a similar temperature range with a view to developing wearable temperature sensors. The temperature coefficient is negative with the value of the same order magnitude as
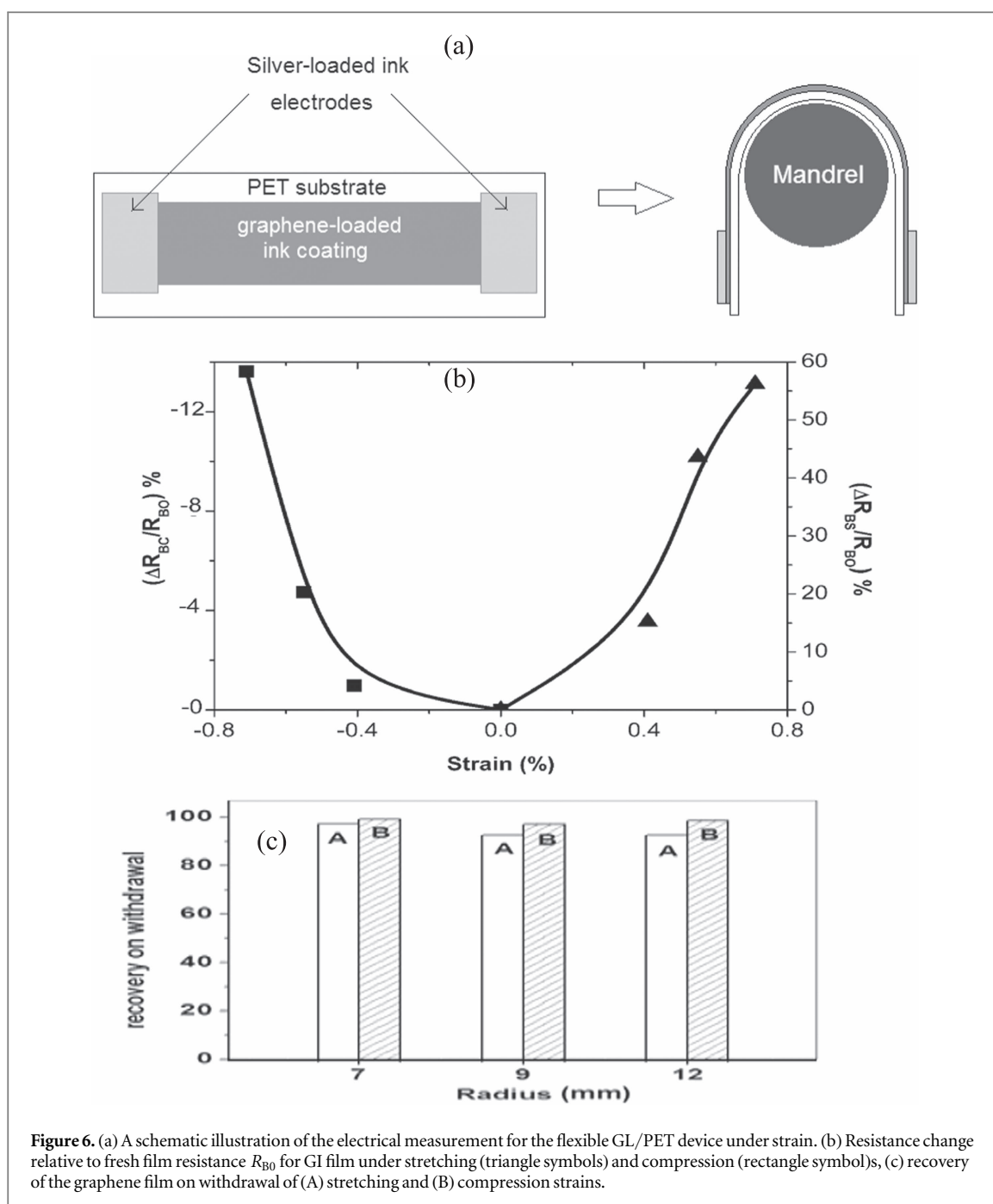
Figure 6. (a) A schematic illustration of the electrical measurement for the flexible GL/PET device under strain. (b) Resistance change relative to fresh film resistance R_{B0} for GI film under stretching (triangle symbols) and compression (rectangle symbol)s, (c) recovery of the graphene film on withdrawal of (A) stretching and (B) compression strains.

obtained in the present investigation, implying the potential applications of the present GI in the development wearable temperature sensors. Also, values of 24.19 and 90.7 meV for activation energies of graphene flake- and solar exfoliated reduced graphene respectively are higher than one obtained in the present drop-cast graphene film, indicating non-metallic characteristics of these graphene [37].

3.3. Electrical properties under bending stress

The bending is commonly applied as strain for uniaxial tensile stress. As shown in figure 6(a), the strain was applied parallel to the length of the film so that the electrodes were not subjected to any strain. The strain is estimated in percentage from the

knowledge of the substrate thickness and radius of curvature. Three radii of curvature of 2, 7 and 12 nm were used. Figure 6(b) shows the results of the bending test in terms of percentage change of resistances, $\left(\frac{\Delta R_{BS}}{R_{B0}}\right)$ due to stretching. R_{B0} is the fresh film resistance prior to application of any stretching and compression stress and $\Delta R_{BS} = R_{BS} - R_{B0}$ where R_{BS} is the resistance of the strained film. $\frac{\Delta R_{BS}}{R_{B0}}$ is found to increase with increasing strain, implying an increase in the resistance (R_{BS}) on stretching. Similar behaviour was reported for CVD grown graphene layers [38]. Phenomenologically, the stretching causes the increase in length of the film with simultaneous decrease in its thickness and both these dimensional
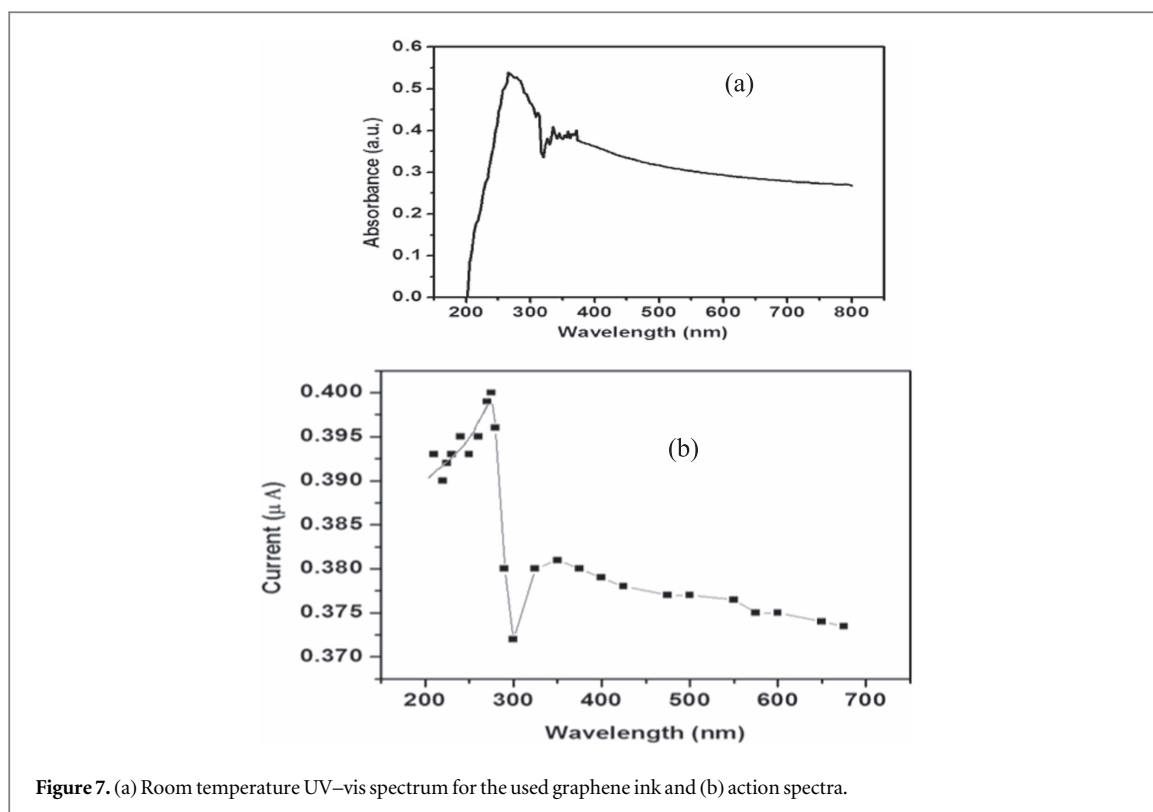
Figure 7. (a) Room temperature UV–vis spectrum for the used graphene ink and (b) action spectra.

changes contribute to the increase in Ohmic resistance on stretching. The Dirac points in the strained graphene are believed to have undergone displacement from the K points, possibly opening up the energy gap. The GI film surface may be not completely flat because of imperfect adhesion to the PET substrate. The scattering of charges due to the non-flat nature of the strained GI surface may also contribute to the increase in resistance [39]. The measurements were repeated on the same film under compression over the same strain range and the results are also illustrated in figure 6(b) in the terms of the dependence of $\left(\frac{\Delta R_{BC}}{R_{B0}}\right)$ on the compressing strain where $\Delta R_{BC} = R_{BC} - R_{B0}$ in which R_{BC} is the resistance of the compressed film. As expected, the resistance is found to decrease with the increase in the strain. The opposite dimensional changes of the films occur on compression, reducing the Ohmic film resistances. In order to investigate the repeatability of the gauge performance, the resistance of the film (R_{Bw}) was measured after the withdrawal of bending stresses and the magnitude of recovery was estimated as the ratio $\left(\frac{R_{Bw}}{R_{B0}}\right)$ and it is evident from figure 6(c), values of this ratio lie between 97% and 92% as the strain is reduced from 0.71% to 0.41% and the recovery is consistent between both stretched and compressed films. These results indicate a very good degree of the flexibility of the GI films, leading to possible application of these flexible GI films in resistance strain gauges for measuring strain within the range from 0.41% to 0.71%.

3.4. Photoresponse studies

The UV–vis absorption spectrum in figure 7(a) for the graphene film is due to for these interband transitions showing a pronounced and asymmetric peak at 270 nm [40]. This peak position is in close agreement with that observed for films deposited from n-methyl-2-pyrrolidone and ethanol/water based dispersions [11]. The peak is due to a van Hove singularity in the density of states, which occurs close to the hopping energy [41, 42]. The considerable red-shift with respect to the absorption peak of graphene oxide at 226 nm implies reduced disruption of the π-conjugation in the multi-layered graphene film [43]. The flat absorption band over the visible region results from the linear dispersion of Dirac electrons in graphene. The weak broad absorption band (shoulder) around 353 nm corresponds to residual graphitic sp^2 domains in the samples. However, other structural parameters like the number of graphitic layers, curvature of aromatic layers, crystallite size and so on, also affect the shifting of (π–π*) bond position. The action spectrum in figure 7(b) shows the dependence of photocurrent on the incident wavelength, at a fixed bias of 50 mV. As expected, it shows close similarities to the UV–vis absorption spectrum, with a sharp peak occurring at 270 nm. The minor differences may be attributed to scattering and recombination of charges in the GI film.

Figure 8(a) shows $I(V)$ characteristics from a GI sample recorded between ±10 mV were recorded at $T = 268$ K and $T = 330$ K under illumination of a
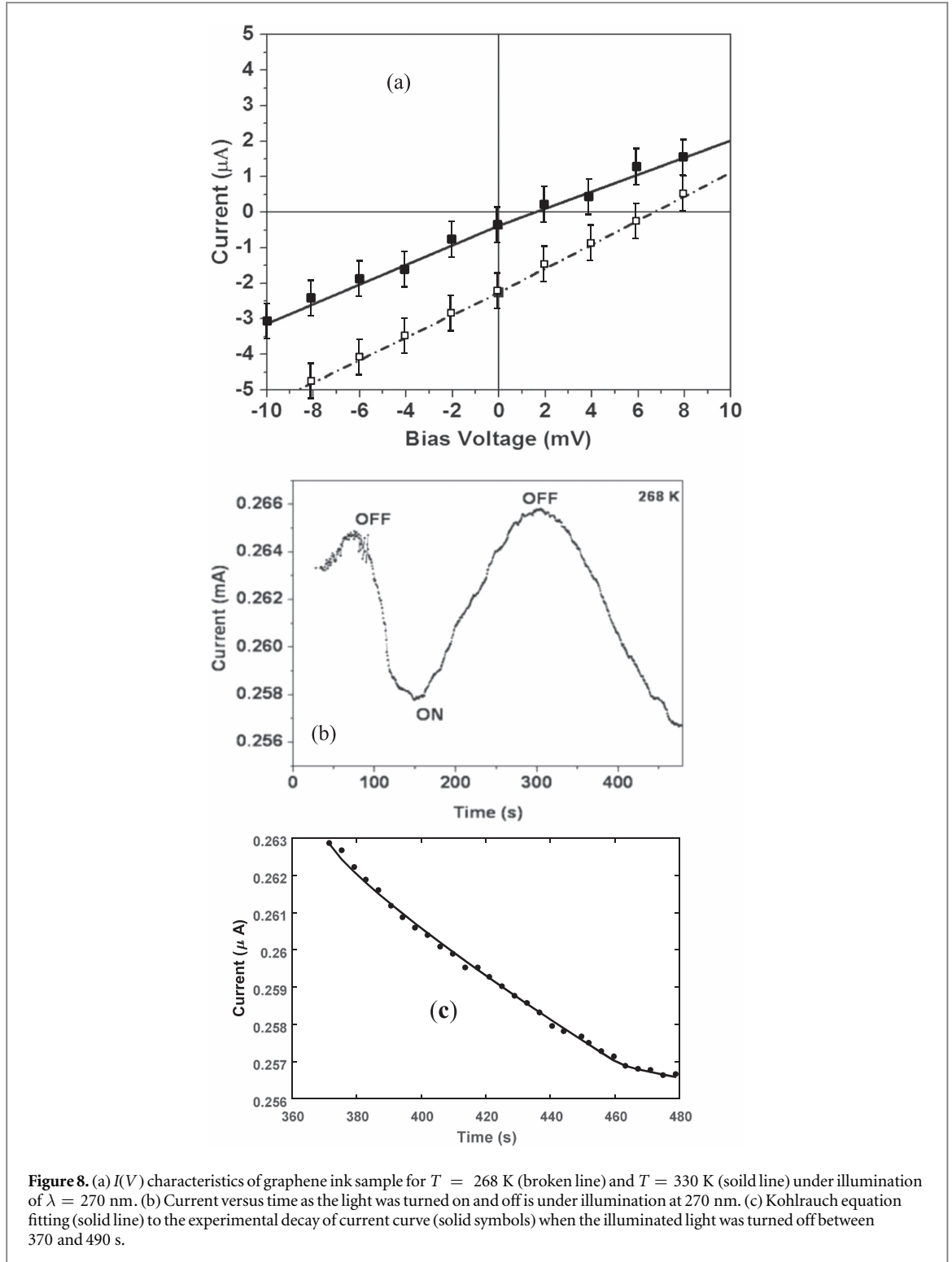
Figure 8. (a) $I(V)$ characteristics of graphene ink sample for $T = 268$ K (broken line) and $T = 330$ K (soild line) under illumination of $\lambda = 270$ nm. (b) Current versus time as the light was turned on and off is under illumination at 270 nm. (c) Kohlrauch equation fitting (solid line) to the experimental decay of current curve (solid symbols) when the illuminated light was turned off between 370 and 490 s.

constant light intensity $P_i = 10$ m Wm^2 corresponding to the absorption peak at 270 nm. The resulting plots were found to be linear for both temperatures. Values of photoconductivity σ_{ph} are estimated to be 8.05 ± 0.67 S m^{-1} and 2.8 ± 0.16 S m^{-1} at 268 K and 330 K, respectively using the following relation:

$$\sigma_{ph} = \frac{R_D - R_{il}}{R_D R_{il}} \frac{d(N-1)}{t.w}, \qquad (5)$$

where R_{il} is the resistance for the GI sample under illumination.

This decrease in σ_{ph} by a factor of nearly 3 with an increase in temperature of 62 K from 268 to 330 K may be interpreted by the photo-thermoelectric effect due to a temperature gradient that is possibly produced between the graphene layers under illumination. The photocurrent in ordinary semiconductors is primarily due to separation of excited electron–hole pairs by a

built-in electric field. A photoexcited *e–h* pair leads to ultrafast heating of the carriers in graphene because of strong *e–e* interactions [44, 45].

The photoresponsivity, *S*, is defined as the ratio of the photocurrent to the incident optical power P_i. Therefore *S* can explicitly be written for the inter-digitated electrode system in the form:

$$S = \frac{t \cdot w}{d^2 N(N-1)} \frac{V\sigma_{ph}}{P_i}. \tag{6}$$

The value of photosensitivity *S* at 268 K is estimated to be 161 A W^{-1} from equation (6). As the temperature is raised to 330 K, *S* is found to decrease to 56 A W^{-1}. This value is of the same order of magnitude as one obtained for the hybrid films containing graphene quantum dots in the reduced graphene oxide matrix [46]. The specific detectivity *D*, can be estimated from the knowledge of *S* using the expression

$$D = \frac{S}{\sqrt{(2q\sigma_D tw / (d(N-1)))}}, \tag{7}$$

where $q = 1.6 \times 10^{-19}$ C is the absolute value of electronic charge. Using the expression above, values of 4.9×10^{12} Jones and 1.9×10^{12} Jones were estimated from equation (7) at 268 K and 330 K, respectively. These values of the specific detectivity represent the capability of the devices to detect a small photo signal.

Values of the short circuit current I_{sc} at zero bias, $V = 0$, are found to be 2.0 μA and 0.4 μA at 268 K and 300 K, respectively, indicating that the number of photo-generated charges are smaller at higher temperatures for a given illumination strength [47]. Similarly, values of 6.7 mV and 1.6 mV are estimated for open circuit voltage V_{oc} using $I = 0$ for 268 K and 300 K, respectively. Figure 8(b) shows a typical current versus time cycle for a fixed bias of 1 V as the light was turned on and off. Two conducting states, high and low, of the GI films are found to exist under illumination and the recovery to nearly low conducting occurs when the illumination is switched off. The response time τ_R is estimated to be 42 s from fitting the exponential function $i = i_0 \left[1 - \exp\left(-\frac{t}{\tau_R}\right) \right]$ to experimental rise curve in figure 8(b), where i_0 is the saturation photocurrent for $t = 0$ at which instant light illumination was switched on at 150 s. This value is found to be comparable with those obtained for the UV sensors based upon reduced graphene oxide decorated ZnO nanostructures [48]. Figure 8(c) presents the results of the analysis of the time-dependent decay of the photocurrent current in terms of the Kohlrauch equation in the form:

$$i(t) = i_0 \exp\left(-\left(\frac{t}{\tau_D}\right)^\gamma\right), \tag{8}$$

where i_0 is the saturation photocurrent for $t = 0$ at which instant light illumination is switched off. The stretching parameter γ normally varies between values of 0 and 1. For $\gamma = 1$, the function in equation (6) approaches classical single-exponential behaviour and differences in energy transfer processes become indistinguishable under this condition [49]. It is obvious that the decay curve in the present work is characterised by two regimes corresponding to (i) fast and (ii) slow relaxation processes. Values of the relaxation time constant, τ_D, were found to be 8.9×10^3 s and 4.3×10^4 s for the time scale regime (i) from 371 s to 463 s and (ii) from 463 s to 482 s respectively by fitting equation (8) to the experimental data. The present $\gamma = 0.82$ may be ascribed to the combined effect of both defects and potential barriers between the edges of the single sheets within the overall assemblies [50].

4. Concluding remarks

A low cost, easy fabrication method has been developed for depositing graphene films on flexible substrates and their optoelectronic properties have been investigated for practical applications. The films studied in this article could be deposited using for example rotary screen-printing, gravure or even offset lithography which are high-speed, volume manufacturing processes. The graphene film in the present investigation is composed of multiple, randomly distributed graphene nano-sheets, in contrast to CVD produced graphene which is typically continuous layers grown directly onto a substrate. It should also be noted that a polymer binder is added to the ink. A value of 3.07×10^{-3} K^{-1} for the positive temperature coefficient of resistivity of the graphene film is comparable to that of common metals like copper and silver and these graphene films may therefore be employed in the manufacture of thermistors for their uses as electronic components in resettable control circuits. The graphene films show a high specific detectivity, of the order of 10^{12} at its maximum absorbance wavelength of 270 nm under a constant light intensity of 10 m W m^{-2}. Two distinct high and low resistive states have been observed. The observation that the properties of our films are similar to 'real' graphene is important because these results may lead to potential exploitation for low cost, large-scale industrially development of highly efficient, large area UV sensors using printed graphene films. Future work will include optimisation of the deposition (printing) procedure to obtain uniform films and investigation into the effect of different polymer binders with a view to improving the mechanical and chemical stability of the film. The graphene content relative to that of polymer binder and the nature of the binder will be interesting features of further investigations into design and fabrication of resistance strain gauges. It may then be possible to improve the recovery performance by using a binder with better elasticity for strain gauge transducers.

Acknowledgments

References

[1] Jang H, Park Y J, Chen X, Das T, Kim M S and Ahn J H 2016 Graphene-based flexible and stretchable electronics *Adv. Mater.* **28** 4184–202

[2] Trung T Q and Lee N E 2016 Flexible and stretchable physical sensor integrated platforms for wearable human-activity monitoring and personal healthcare *Adv. Mater.* **28** 4338–72

[3] Nguyen B H and Nguyen V H 2016 Promising applications of graphene and graphene-based nanostructures *Adv. Nat. Sci.-Nanosci. Nanotechnol.* **7** 023002

[4] Novoselov K S, Geim A K, Morozov S V, Jiang D, Zhang Y, Dubonos S V, Grigorieva I V and Firsov A A 2004 Electric field effect in atomically thin carbon films *Science* **306** 666–9

[5] Wu B, Tuncer H M, Katsounaros A, Wu W P, Matthew T C, Ying K, Zhang L H, Milne W I and Hao Y 2011 Microwave absorption and radiation from large-area multilayer CVD graphene *Carbon* **77** 814–22

[6] Ahmadi S and Afzalzadeh R 2016 Few-layer graphene growth from polystyrene as solid carbon source utilizing simple APCVD method *Physica* E **81** 302–7

[7] Joucken F *et al* 2015 Charge transfer and electronic doping in nitrogen-doped graphene *Sci. Rep.* **5** 14564

[8] Kang M H, Milne W I and Cole M T 2015 Doping stability and opto-electronic performance of chemical vapour deposited graphene on transparent flexible substrates *IET Circuits Devices Syst.* **9** 39–45

[9] Zhang Y B, Tang T T, Girit C, Hao Z, Martin M C, Zettl A, Crommie M F, Shen Y R and Wang F 2009 Direct observation of a widely tunable bandgap in bilayer graphene *Nature* **459** 820–3

[10] Kong D, Le L T, Li Y, Zunino J L and Lee W 2012 Temperature-dependent electrical properties of graphene inkjet-printed on flexible materials *Langmuir* **28** 13467–72

[11] Capasso A, Castillo A E D, Sun H, Ansaldo A, Pellegrini V and Bonaccorso F 2015 Ink-jet printing of graphene for flexible electronics: an environmentally-friendly approach *Solid State Commun.* **224** 53–63

[12] Chen G H, Wu D J, Weng W U and Wu C L 2003 Exfoliation of graphite flake and its nanocomposites *Carbon* **41** 619–21

[13] Majee S, Song M, Zhang S L and Zhang Z B 2016 Scalable inkjet printing of shear-exfoliated graphene transparent conductive films *Carbon* **102** 51–7

[14] Nebogatikova N A, Antonova I V, Kurkina I I, Soots R A, Vdovin V I, Timofeev V B, Smagulova S A and Prinz V Y 2016 Fluorinated graphene suspension for inkjet printed technologies *Nanotechnology* **27** 205601

[15] Zhang Q Q, Zhang F, Medarametla S P, Li H, Zhou C and Lin D 2016 3D printing of graphene aerogels *Small* **12** 1702–8

[16] Banerjee I, Faris T, Stoeva Z, Sharma A K and Ray A K 2016 Printed graphene films with positive temperature coefficient of resistivity *Mater. Today: Proc.* **3** 4035–39

[17] Dang V Q, Trung T Q, Kim D I, Duy L T, Hwang B U, Lee D W, Kim B Y, Toan L D and Lee N E 2015 Ultrahigh responsivity in graphene-ZnO nanorod hybrid UV photodetector *Small* **11** 3054–65

[18] Luo J, Tian P, Pan C T, Robertson A W, Warner J H, Hill E W and Briggs G A D 2011 Ultralow secondary electron emission of graphene *ACS Nano* **5** 1047–55

[19] Guo H L, Wang X F, Qian Q Y, Wang F B and Xia X H 2009 A green approach to the synthesis of graphene nanosheets *ACS Nano* **3** 2653–9

[20] Huh S H 2014 X-ray diffraction of multi-layer graphenes: instant measurement and determination of the number of layers *Carbon* **78** 617–21

[21] Toh S Y, Loh K S, Kamarudin S K and Daud W R W 2014 Graphene production via electrochemical reduction of graphene oxide: synthesis and characterisation *Chem. Eng. J.* **251** 422–34

[22] Torrisi F *et al* 2012 Inkjet-printed graphene electronics *ACS Nano* **6** 2992–3006

[23] Ferrari A C 2007 Raman spectroscopy of graphene and graphite: disorder, electron–phonon coupling, doping and nonadiabatic effects *Solid State Commun.* **143** 47–57

[24] Eckmann A, Felten A, Verzhbitskiy I, Davey R and Casiraghi C 2013 Raman study on defective graphene: effect of the excitation energy, type, and amount of defects *Phys. Rev.* B **88** 035426

[25] Ferrari A C and Basko D M 2013 Raman spectroscopy as a versatile tool for studying the properties of graphene *Nat. Nanotechnol.* **8** 235–46

[26] Ni Z H, Wang Y Y, Yu T, Yu and Shen Z X 2008 Raman spectroscopy and imaging of graphene *Nano Res.* **1** 273–91

[27] Ferrari A C *et al* 2006 Raman spectrum of graphene and graphene layers *Phys. Rev. Lett.* **97** 187401

[28] Rider A N, An Q, Thostenson E T and Brack N 2014 Ultrasonicated-ozone modification of exfoliated graphite for stable aqueous graphitic nanoplatelet dispersions *Nanotechnology* **25** 495607

[29] Wu Y P, Wang B, Ma Y F, Huang Y, Li N, Zhang F and Chen Y S 2010 Efficient and large-scale synthesis of few-layered graphene using an arc-discharge method and conductivity studies of the resulting films' *Nano Res.* **3** 661–9

[30] Giardi R, Porro S, Chiolerio A, Celasco and Sangermano M 2013 'Inkjet printed acrylic formulations based on UV-reduced graphene oxide nanocomposites' *J. Mater. Sci.* **48** 1249–55

[31] Yang J, Wei D P, Tang L L, Song X F, Luo W, Chu J, Gao T P, Shi H F and Du C L 2015 Wearable temperature sensor based on graphene nanowalls *RSC Adv.* **5** 25609–15

[32] Giancoli D C 1995 *Physics* 4th edn (Englewood Cliffs, NJ: Prentice-Hall)

[33] Tian M, Huang Y, Wang W H, Li R Q, Liu P, Liu C X and Zhang Y G 2014 Temperature-dependent electrical properties of graphene nanoplatelets film dropped on flexible substrates *J. Mater. Res.* **29** 1288–94

[34] Borysenko K M, Mullen J T, Barry E A, Paul S, Semenov Y G, Zavada J M, Nardelli M B and Kim K W 2010 First-principles analysis of electron–phonon interactions in graphene *Phys. Rev.* B **81** 121412

[35] Yavari F, Kritzinger C, Gaire C, Song L, Gullapalli H, Borca-Tasciuc T, Ajayan P M and Koratkar N 2010 Tunable bandgap in graphene by the controlled adsorption of water molecules *Small* **6** 2535–8

[36] Dvorak M, Oswald W and Wu Z G 2013 Bandgap opening by patterning graphene *Sci. Rep.* **3** 2289

[37] Sahatiya P, Puttapati S K, Srikanth V V S S and Badhulika S 2016 Graphene-based wearable temperature sensor and infrared photodetector on a flexible polyimide substrate *Flex. Print. Electron.* **1** 025006

[38] Lee Y H and Kim Y J 2012 Electrical and lattice vibrational behaviors of graphene devices on flexible substrate under small mechanical strain *Appl. Phys. Lett.* **101** 083102

[39] Haniff M A S M, Hafiz S M, Wahid K A A, Endut Z, Lee H W, Bien D C S, Azid I A, Abdullah M Z, Huang N M and Rahman S A 2015 Piezoresistive effects in controllable defective HFTCVD graphene-based flexible pressure sensor *Sci. Rep.* **5** 14751

[40] Lee C, Leconte N, Kim J, Cho D, Lyo I W and Choi E J 2016 Optical spectroscopy study on the effect of hydrogen adsorption on graphene *Carbon* **103** 109–14

[41] Mak K F, Ju L, Wang F and Heinz T F 2012 Optical spectroscopy of graphene: from the far infrared to the ultraviolet *Solid State Commun.* **152** 1341–9

[42] Kravets V G, Grigorenko A N, Nair R R, Blake P, Anissimova S, Novoselov K S and Geim A K 2010 Spectroscopic ellipsometry of graphene and an exciton-shifted van Hove peak in absorption *Phys. Rev.* B **81** 155413

[43] Sur U K, Saha A, Datta A, Ankamwar B, Surti F, Roy S D and Roy D 2016 Synthesis and characterization of stable aqueous dispersions of graphene *Bull. Mater. Sci.* **39** 159–65

[44] Xu X D, Gabor N M, Alden J S, van der Zande A M and McEuen P L 2010 Photo-thermoelectric effect at a graphene interface junction *Nano Lett.* **10** 562–6

[45] Koppens F H L, Mueller T, Avouris P, Ferrari A C, Vitiello M S and Polini M 2014 Photodetectors based on graphene, other two-dimensional materials and hybrid systems *Nat. Nanotechnol.* **9** 780–93

[46] Tam T V, Hur S H, Chung J S and Choi W M 2015 Ultraviolet light sensor based on graphene quantum dots/reduced graphene oxide hybrid film *Sensors Actuators* A **233** 368–73

[47] Sun R J, Zhang Y, Li K, Hui C, He K, Ma X C and Liu F 2013 Tunable photoresponse of epitaxial graphene on SiC *Appl. Phys. Lett.* **103** 013106

[48] Wang Z X, Zhan X Y, Wang Y J, Muhammad S, Huang Y and He J 2012 A flexible UV nanosensor based on reduced graphene oxide decorated ZnO nanostructures *Nanoscale* **4** 2678–84

[49] Covington L R and Moore J C 2013 Photoconductivity and transient response of Al:ZnO: Al planar structures fabricated via a thermal oxidation process *Thin Solid Films* **540** 106–11

[50] Loomis J and Panchapakesan B 2012 Large photocurrents in single layer graphene thin films: effects of diffusion and drift *Nanotechnology* **23** 265203